Live imaging using adaptive optics with fluorescent protein guide-stars

Xiaodong Tao,[1,*] Justin Crest,[2] Shaila Kotadia,[2] Oscar Azucena,[1] Diana C. Chen,[3] William Sullivan,[2] and Joel Kubby[1]

[1]*W.M. Keck Center for Adaptive Optical Microscopy, Jack Baskin School of Engineering, University of California, Santa Cruz, California 95064, USA*
[2]*Molecular, Cell, and Developmental Biology, University of California, Santa Cruz, California 95064, USA*
[3]*Lawrence Livermore National Laboratory, Livermore, California 94550, USA*
**taoxd@soe.ucsc.edu*

Abstract: Spatially and temporally dependent optical aberrations induced by the inhomogeneous refractive index of live samples limit the resolution of live dynamic imaging. We introduce an adaptive optical microscope with a direct wavefront sensing method using a Shack-Hartmann wavefront sensor and fluorescent protein guide-stars for live imaging. The results of imaging *Drosophila* embryos demonstrate its ability to correct aberrations and achieve near diffraction limited images of medial sections of large Drosophila embryos. GFP-polo labeled centrosomes can be observed clearly after correction but cannot be observed before correction. Four dimensional time lapse images are achieved with the correction of dynamic aberrations. These studies also demonstrate that the GFP-tagged centrosome proteins, Polo and Cnn, serve as excellent biological guide-stars for adaptive optics based microscopy.

OCIS codes: (110.1080) Active or adaptive optics; (010.7350) Wave-front sensing; (180.2520) Fluorescence microscopy; (180.6900) Three-dimensional microscopy; (170.3880) Medical and biological imaging.

References and links

1. M. J. Booth, "Adaptive optics in microscopy," Phil. Trans. R. Soc. A–Math. Phys. Eng. Sci. **365**, 2829–2843 (2007).
2. R. K. Tyson, *Principles of Adaptive Optics* (Academic, 1991).
3. J. Porter, H. Queener, J. Lin, K. Thorn, and A. A. S. Awwal, *Adaptive Optics for Vision Science: Principles, Practices, Design and Applications*, (Wiley, 2006).
4. P. Marsh, D. Burns, and J. Girkin, "Practical implementation of adaptive optics in multiphoton microscopy," Opt. Express **11**(10), 1123–1130 (2003).
5. D. Débarre, E. J. Botcherby, T. Watanabe, S. Srinivas, M. J. Booth, and T. Wilson, "Image-based adaptive optics for two-photon microscopy," Opt. Lett. **34**(16), 2495–2497 (2009).
6. N. Olivier, D. Débarre, and E. Beaurepaire, "Dynamic aberration correction for multiharmonic microscopy," Opt. Lett. **34**(20), 3145–3147 (2009).
7. A. Facomprez, E. Beaurepaire, and D. Débarre, "Accuracy of correction in modal sensorless adaptive optics," Opt. Express **20**(3), 2598–2612 (2012).
8. M. Rueckel, J. A. Mack-Bucher, and W. Denk, "Adaptive wavefront correction in two-photon microscopy using coherence-gated wavefront sensing," Proc. Natl. Acad. Sci. U.S.A. **103**(46), 17137–17142 (2006).
9. N. Ji, D. E. Milkie, and E. Betzig, "Adaptive optics via pupil segmentation for high-resolution imaging in biological tissues," Nat. Methods **7**(2), 141–147 (2010).
10. D. E. Milkie, E. Betzig, and N. Ji, "Pupil-segmentation-based adaptive optical microscopy with full-pupil illumination," Opt. Lett. **36**(21), 4206–4208 (2011).
11. M. J. Booth, M. A. Neil, R. Juskaitis, and T. Wilson, "Adaptive aberration correction in a confocal microscope," Proc. Natl. Acad. Sci. U.S.A. **99**(9), 5788–5792 (2002).
12. O. Azucena, J. Crest, S. Kotadia, W. Sullivan, X. Tao, M. Reinig, D. Gavel, S. Olivier, and J. Kubby, "Adaptive optics wide-field microscopy using direct wavefront sensing," Opt. Lett. **36**(6), 825–827 (2011).
13. X. Tao, B. Fernandez, O. Azucena, M. Fu, D. Garcia, Y. Zuo, D. C. Chen, and J. Kubby, "Adaptive optics confocal microscopy using direct wavefront sensing," Opt. Lett. **36**(7), 1062–1064 (2011).
14. X. Tao, O. Azucena, M. Fu, Y. Zuo, D. C. Chen, and J. Kubby, "Adaptive optics microscopy with direct wavefront sensing using fluorescent protein guide stars," Opt. Lett. **36**(17), 3389–3391 (2011).

#166370 - $15.00 USD Received 23 Apr 2012; revised 18 Jun 2012; accepted 19 Jun 2012; published 28 Jun 2012

15. R. Aviles-Espinosa, J. Andilla, R. Porcar-Guezenec, O. E. Olarte, M. Nieto, X. Levecq, D. Artigas, and P. Loza-Alvarez, "Measurement and correction of in vivo sample aberrations employing a nonlinear guide-star in two-photon excited fluorescence microscopy," Biomed. Opt. Express **2**(11), 3135–3149 (2011).
16. O. Azucena, X. Tao, J. Crest, S. Kotadia, W. Sullivan, D. Gavel, M. Reinig, S. Olivier, and J. Kubby, "Adaptive optics wide-field microscope corrections using a MEMS DM and Shack-Hartmann wavefront sensor," Proc. SPIE **7931**, 79310J (2011).
17. M. Gu, *Advanced Optical Imaging Theory* (Springer-Verlag, New York, 1999).
18. S. Thomas, T. Fusco, A. Tokovinin, M. Nicolle, V. Michau, and G. Rousset, "Comparison of centroid computation algorithms in a Shack-Hartmann sensor," Mon. Not. R. Astron. Soc. **371**(1), 323–336 (2006).
19. L. A. Poyneer, D. T. Gavel, and J. M. Brase, "Fast wave-front reconstruction in large adaptive optics systems with use of the Fourier transform," J. Opt. Soc. Am. A **19**(10), 2100–2111 (2002).
20. M. Gu, *Principles of Three-Dimensional Imaging in Confocal Microscopes* (World Scientific, Singapore, 1996).
21. J. W. Hardy, *Adaptive Optics for Astronomical Telescopes* (Oxford University Press, 1998).
22. M. Schwertner, M. J. Booth, M. A. Neil, and T. Wilson, "Measurement of specimen-induced aberrations of biological samples using phase stepping interferometry," J. Microsc. **213**(1), 11–19 (2004).
23. O. Azucena, J. Crest, J. Cao, W. Sullivan, P. Kner, D. Gavel, D. Dillon, S. Olivier, and J. Kubby, "Wavefront aberration measurements and corrections through thick tissue using fluorescent microsphere reference beacons," Opt. Express **18**(16), 17521–17532 (2010).
24. L. A. Poyneer and B. A. Macintosh, "Spatially filtered wave-front sensor for high-order adaptive optics," J. Opt. Soc. Am. A **21**(5), 810–819 (2004).
25. J. Zhang and T. L. Megraw, "Proper recruitment of gamma-tubulin and D-TACC/Msps to embryonic Drosophila centrosomes requires Centrosomin Motif 1," Mol. Biol. Cell **18**(10), 4037–4049 (2007).
26. T. Moutinho-Santos, P. Sampaio, I. Amorim, M. Costa, and C. E. Sunkel, "In vivo localisation of the mitotic POLO kinase shows a highly dynamic association with the mitotic apparatus during early embryogenesis in Drosophila," Biol. Cell **91**(8), 585–596 (1999).
27. W. F. Rothwell and W. Sullivan, "Fluorescent analysis of drosophila embryos," in *Drosophila Protocols*, W. Sullivan, M. Ashburner and R. S. Hawley, eds. (Cold Spring Harbor Laboratory Press, 2000), pp. 141–157.

1. Introduction

The ability to see within live biological tissues at the cellular-level using optical microscopes benefits a wide range of biological research fields such as neural science and developmental biology. However, the penetration depth for currently available systems is still limited. One of the important issues is the aberration induced by the inhomogeneous refractive index of tissue [1]. Different from the predictable aberration induced from the cover slides and/or mounting medium, the tissue induced aberration is highly dependent on the spatial location in the sample. The cellular motions in live dynamic tissue further increase the uncertainty of aberration. The conventional methods to pre-compensate the spherical aberration by adding a correction collar on the objective lens or integrating a specially designed lens group cannot solve this issue. Similar issues also hinder the imaging capabilities of other systems. Atmospheric turbulence induced aberrations for example, limits the resolving power of terrestrial telescopes [2]. The successful applications of adaptive optics (AO) in ground-based telescopes to compensate dynamic aberrations are leading researchers to apply AO to other fields such as vision science and microscopy. The typical AO system includes a wavefront sensor for measuring the distorted wavefront and a wavefront corrector, such as a deformable mirror (DM) or a spatial light modulator, to correct the aberration in a feedback loop. The requirement of a reference point-source behind the inhomogeneous medium, also called a "guide-star", for wavefront measurement restricts its application. AO systems in vision science found their guide-star from the stable reflection off of the retina which expedited its transformation from the research stage to clinical applications [3]. Unfortunately for AO microscopy (AOM), it is not straightforward to find a guide-star in biological tissue. To circumvent this issue, most of the AOMs apply indirect methods for wavefront measurement which depend on processing of the final image [4, 5]. Numerous iterations are required to find the wavefront, which will cause photobleaching and limit the bandwidth of imaging. Image based methods have been applied in third-harmonic generation microscopy for live imaging [6]. By using image sharpness as an image quality metric, the correction of N aberration modes requires 2(2N + 1) measurements to correct the dynamic aberration. Image based methods were investigated in detail in [7]. A direct wavefront sensing method using backscattered light has been used in a two-photon microscope [8], which is highly dependent on the backscattering efficiency of the tissue. Its complex procedure makes it computationally

#166370 - $15.00 USD Received 23 Apr 2012; revised 18 Jun 2012; accepted 19 Jun 2012; published 28 Jun 2012

intensive. Other approaches use a direct wavefront measurement based on sequential measurements of the wavefront error in each segment of the aperture [9, 10], or sequential intensity measurements with different trial aberrations [11]. Both of these serial approaches limit their application in live imaging for observation of fast dynamic events. To achieve a stable and accurate wavefront measurement and correction, we previously introduced a direct wavefront sensing method using injected fluorescent microspheres as reference sources for a Shack-Hartmann wavefront sensor (SHWS) [12,13]. We further tested fluorescent proteins (FPs) in a fixed mouse brain tissue as a laser guide-star source [14]. As a non-invasive and high-speed method, it shows the potential application in live imaging. A similar setup using a combination of wavefront-sensor and deformable mirror in two photon microscopy has been reported in [15]. The near-infrared lasers for two-photon excitation provide deeper penetration. It shows intensity and contrast improvements but resolution improvements near the diffraction limit have not been shown. Moreover the compensation of the wavefront using the SHWS for live imaging of fast dynamic processes in biological samples has not been reported. Here we present a specially designed AOM using fluorescent protein centrosome guide-star (FPCGS) for the first dynamic aberration correction using a SHWS for imaging of a developing embryo. The dynamic motion of the sample requires the system to locate the guide-star, measure and correct the wavefront error in a short time period. To minimize the chance of photobleaching and phototoxic effects, it requires short exposure time for generating a guide-star. This paper suggests using a protected closed-loop wavefront correction method to achieve shorter sample exposure time during wavefront correction. The guide-star searching algorithm can find the best guide-star based on the intensity. The whole process is automated and synchronized with the image scanning process to provide four dimensional time lapse images with the correction of dynamic aberrations. The total wavefront correction time is 600 ms. It includes 500 ms for switching the flipper mirror, The switching time can be further minimized to less than 1ms by using a fast steering mirror.

2. Setup and method

2.1 System setup and operation

In the AOM, the AO system was integrated into a laser scanning confocal microscope as shown in Fig. 1(a). The AO system includes a DM and a SHWS. The mirror was initially flattened using an interferometer and a custom software program. After calibrating the flat surface, a file of voltages is used to flatten the mirror during operation. The system aberrations are corrected before the operation. The excitation of FPCGS is accomplished by steering the excitation light from a solid state laser (488 nm) onto the FPCGS in the object plane. The emission light from the guide-star is used to measure and correct the wavefront aberrations induced by the tissue on the optical path. For live imaging, focusing the laser on a moving FPCGS is challenging. For feedback control of the DM, several iterations are needed to make a full correction, which requires the laser to focus on the guide-star during correction. Although an increase of the laser power may decrease the exposure time for wavefront sensing, it also increases the chance of photobleaching. To overcome this issue, a protected closed-loop control of the DM is applied with only a single sample exposure for a full wavefront correction. This method does not need a complex DM calibration process, which simplifies the implementation of the system. Optical paths of the AOM have three configurations for confocal imaging, wavefront measurements and protected closed-loop control of the DM respectively, which are controlled by two motorized flip mirrors (M1 and M2) to accomplish an AO correction in four steps:

(i) In *confocal imaging without a correction step*, the confocal image is collected with a correction of system aberration. The potential guide-star is found automatically by a FPCGS searching algorithm. The locations of guide-stars are obtained based on the intensity information from the confocal image by a guide-star searching algorithm discussed in Section 2.3.

#166370 - $15.00 USD Received 23 Apr 2012; revised 18 Jun 2012; accepted 19 Jun 2012; published 28 Jun 2012

(ii) Then in the wavefront measurement step, the scanners steer the beam to the desired FPCGS and the flip mirror (M1) reflects the emission light from the guide-star to the wavefront sensor. The wavefront is reconstructed and saved in the control system.

(iii) In the protected closed-loop control step, the flip mirror (M2) moves into the optical path. The DM is controlled using the reference laser and the SHWS and a wavefront which is opposite to the measured wavefront is generated. A more detailed description is provided in Section 2.2.

(iv) Finally, the confocal image with correction is collected with the two flip mirrors out of the light path. As can be seen, each wavefront correction only needs a single sample exposure, which is 50 ms long in the current system for imaging of a *Drosophila* embryo. The exposure time for wavefront measurement is short enough to capture enough photons before the guide-star moves away.

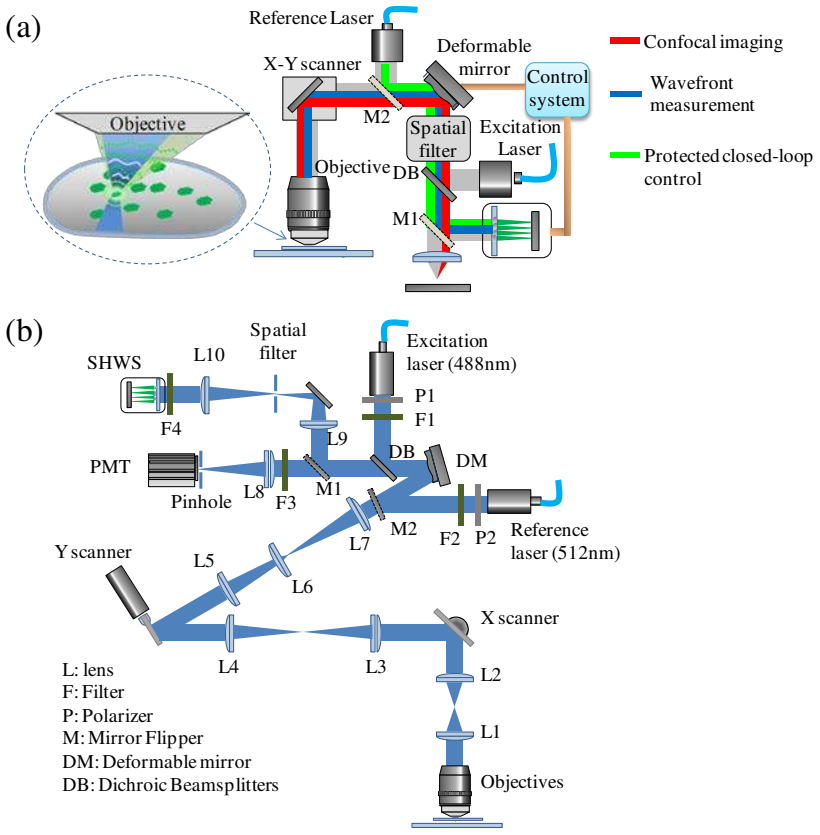

Fig. 1. System setup. (a) Schematic diagram of the AOM: GFPs are illuminated with an excitation laser (488 nm) to produce a guide-star. The reference laser is used for wavefront control. The flip mirrors M1 and M2 control the light path for confocal imaging (red), wavefront measurement (blue) and protected closed-loop control of the DM (green). (b) Experimental set-up of the AOM. L, lens; F, filter; P, polarizer; M, mirror flipper; DM, deformable mirror; DB, dichroic beamplitters.

The detailed configuration of the system is shown in Fig. 1(b). A solid state laser (488 nm, LuxX 488-60, Omicron) is used to excite the green fluorescent protein (GFP) in the *Drosophila* embryo for both confocal imaging and guide-star illumination. The excitation beam passes through an excitation filter (FF02-482/18-25, Semrock) and is reflected by a dichroic beamsplitter (Di01-R488, Semrock). Two galvo scanners (6215H, Cambridge Technology) are used to scan the beam on the sample in a raster pattern. Those scanners can

#166370 - $15.00 USD Received 23 Apr 2012; revised 18 Jun 2012; accepted 19 Jun 2012; published 28 Jun 2012

also steer the beam on the desired FPCGS localized by a guide-star searching algorithm for wavefront sensing. Between the two scanners, a relay lens group (L3 and L4 both with 150 mm focal length, Thorlabs) makes a conjugation for the two scanners, which will minimize the pupil shift on the exit pupil of the objective lens. The exit pupil of the objective is projected onto the X scanner by lens L2 (100 mm focal length) and the tube lens. Lens group L5, L6 and L7 relays the pupil plane onto a DM. The emission light from the sample is descanned by the two scanners and switched by a flip mirror (Thorlabs) between the wavefront sensing and confocal imaging paths. The emission light passes through the dichroic beam splitters and is then further filtered by emission filters F3 and F4 (BLP01-488R, Semrock). For confocal imaging, the emission light is focused by an imaging lens L8 (150 mm focal length, Thorlabs) on a pinhole with the size corresponding to 1 Airy unit (50 μm diameter, Thorlabs), which is conjugate with the object plane. The light is finally collected by a photomultiplier tube (PMT, H7422-40, Hamamatsu). The current output signal from the PMT was amplified and converted to voltage output by a wide band amplifier (C6438-01, Hamamatsu). A custom analog integrator is used to integrate the signal during each pixel dwell time. The signal is finally sampled by a data acquisition board (PCIe-6363, National Instruments). For wavefront sensing, lens group L9 and L10 (250 mm focal length, Thorlabs) relay the pupil plane to the SHWS. The SHWS is composed of a 44x44 element lenslet array with a lens diameter of 400 μm and focal length of 24 mm (AOA Inc., Cambridge, MA) and an electron multiplying charge coupled device (EMCCD) camera (Cascade II, Photometrics). Only 97 lenslets are used inside of a 4.4 mm diameter pupil. To minimize the light coming from the out of focus planes, an iris diaphragm (Edmund Optics) is used as a spatial filter. To correct the aberration induced by the sample, a DM with 140 actuators and 3.5 μm of stroke (Boston Micromachines) is placed in the light path, which is conjugate to the exit pupil of the objective and the wavefront sensor. The Fried configuration is used, where the actuators of the DM are aligned to the center of four neighboring lenslets [3]. For protected closed-loop control of the DM, a reference laser is used as a source to set the shape of the DM. An additional flip mirror (M2) is applied to direct the laser to the system. The intensity of the two lasers can be adjusted by polarizers P1, P2 (Thorlabs) and further tuned by the computer through a software control interface. The custom system was set-up on an optical vibration isolation optical table and uses an inverted microscope frame which includes a 60X water immersion objective with a numerical aperture of 1.1 (Olympus Microscope, Center Valley, PA) and a built-in tube lens L1 (180 mm focal length). A motorized XYZ stage with a piezo Z-axis top plate is installed for precise positioning of the sample and Z scanning for confocal imaging. The optical system is designed, optimized and analyzed by the optical design software CODE V (Optical Research Associates).

2.2 Protected closed- loop control of the DM

To protect the sample from the laser exposure during closed-loop DM control, the protected closed-loop control method was used. Having measured the aberration from the FPCGS, the mirror is commanded to generate the inverse aberration via iterative closed-loop control using a reference laser. By using this configuration, the use of fluorescence light from the sample is minimized to reduce photobleaching and phototoxic effects. The current system takes 50 ms for wavefront measurement and 50 ms for correction. Between intervals, there is another 500 ms for switching the flipper mirror. The control is based on the wavefront slope measurement S_m in the wavefront measurement step and the wavefront slope measurement S_{OL} in the DM control step. The actuator command for the deformable mirror is achieved by the following equation:

$$V = A^{+}(S_m + S_{OL}) \tag{1}$$

where A^{+} is the pseudo-inverse of the slope influence matrix [3]. This will generate a wavefront which is opposite to the one induced by the biological samples.

#166370 - $15.00 USD Received 23 Apr 2012; revised 18 Jun 2012; accepted 19 Jun 2012; published 28 Jun 2012

2.3 Guide-star searching

The guide-star searching algorithm was developed to localize the desired guide-star automatically during confocal imaging process. The flowchart of the algorithm is shown in Fig. 2. The algorithm first initializes the guide-star size R_s, the threshold value T for image threshholding and the maximum star number N_{max}. The number of the detected guide-stars depends on these settings. The noise in the image is first removed using Gaussian filters. The location S_{max} of the global maximum of the image is achieved, which is the first guide-star. The next guide-star can be located by assigning zero to the area of the previous guide-star and searching for the maximum of the modified image. The searching loop stops when the predefined maximum number of guide-stars N_{max} is achieved or the intensity of the star is less than the threshold value T. In searching for the best guide-star, three criteria are available: the brightest guide-star, the star closest to the center of the image and the brightest star in a defined area. For the experiments in this paper, the first criterion was used.

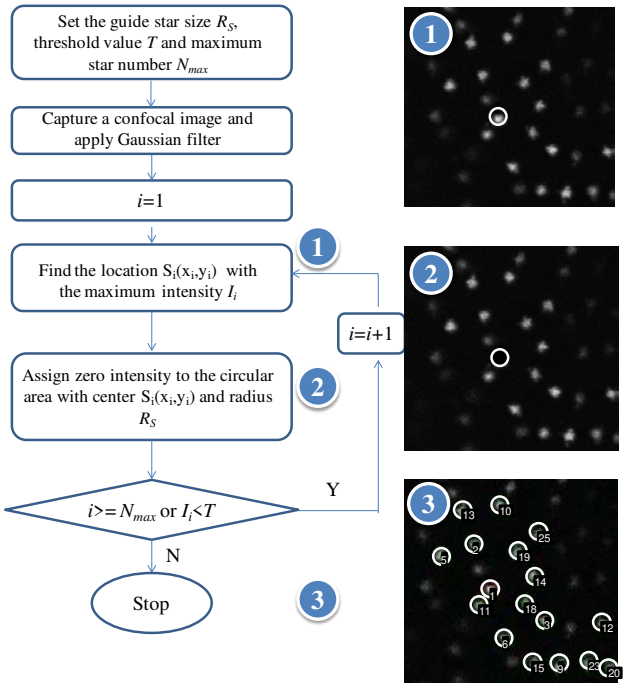

Fig. 2. Flowchart for the guide-star searching algorithm. The algorithm is to search and calculate the locations of the possible guide-stars stars in the image.

2.4 The requirement for the size of the guide-star

To achieve an accurate wavefront measurement, the size of the FPCGS should be small enough to provide a diffraction-limited image on the wavefront sensor. The SHWS consists of a lenslet array and a CCD camera. The local tilt of the wavefront on each lenslet can be estimated from the displacement of the focal spot on the sensor. The whole wavefront error can then be reconstructed from the local slopes. Diffraction limited spots on the sensor are required to make an accurate estimation. Therefore the diameter of the guide-star should be smaller than the diffraction limit of the SHWS defined as [16]

$$d_{diffraction\_limit} = 2.44 \frac{\lambda}{2NA} \frac{D_0}{d_l} \tag{2}$$

#166370 - $15.00 USD Received 23 Apr 2012; revised 18 Jun 2012; accepted 19 Jun 2012; published 28 Jun 2012

where λ is the wavelength, NA and D_0 are the numerical aperture and the pupil diameter on the wavefront sensor, respectively. d_l is the diameter of a lens in the Shack-Hartmann lenslet array. For the current setup, λ = 0.509μm; NA = 1.1; $D_0 = 4 \times 10^3$μm; d_l = 400μm. So $d_{diffraction\_limit}$ is equal to 5.64 μm. For laser scanning fluorescent microscopy, the emission light from a given point on the FP labeled structure is proportional to the light intensity illuminating that point. If the size of the FPs structure is smaller than the illumination PSF, the size of the guide-star is equal to the size of the real structure. If the size of the FPs structure is larger than the PSF, then the size of the guide-star depends on the illumination PSF. In this case, it is like the sodium-layer laser guide-star used in astronomy. The only part of the sodium layer that fluoresces is where it is illuminated by the laser. The illumination PSF is defined as [17]

$$h(x_2, y_2) = \frac{i}{\lambda} \iint_{\Sigma} P(x_1, y_1) \exp[-ik\,\phi(x_1, y_1)] \frac{\exp[-ik\,(r - R)]}{Rr} \cos(n, r) dS \qquad (3)$$

where (x_2,y_2) are the coordinates in the focusing plane. (x_1,y_1) are the coordinates in the pupil plane. $P(x_1,y_1)$ and $\varphi(x_1,x_2)$ are the light field in amplitude and phase, respectively. k is the wave number. n is the unit normal of the pupil plane. r is the unit vector from (x_1,y_1) to (x_2,y_2). R is the distance from the pupil plane to (x_2,y_2). dS is the area element on the pupil plane. λ is the wavelength of the illumination light. The size of the guide-star can be determined by the area of the PSF with 80% encircled energy. In the current system, the guide-star size at the diffraction limit of the wavefront sensor is 5.41 μm. Owing to the high numerical aperture of the objective lens, the guide-star size for the diffraction limit of the wavefront sensor is larger than that of the microscope system in most of the cases. Based on the wavefront measurement in Section 3.2 and Eq. (3), the real star size is calculated as 4.9 μm at a depth of 90 μm for the *Drosophila* embryo. The space between two guide-stars does not affect the wavefront measurement when the illumination PSF is smaller than the diffraction limit of the SHWS If the space is smaller than $d_{diffraction\_limit}$, only one spot can be observed in the subaperture of the wavefront sensor. If it is larger than $d_{diffraction\_limit}$, the intensity of the guide-star which is located outside of the PSF will drop dramatically. The cross-correlation centroiding algorithm [18] used in the wavefront measurement can further minimize the noise generated from the neighboring guide-star. Due to the short exposure time (50 ms) for wavefront measurement, the theoretical maximum speed of the guide-star motion in the lateral plane can be as high as 49 μm/s at a depth of 90 μm. In the extreme case, when the FPs structure is larger than the illumination PSF and the size of the illumination PSF is larger than the diffraction limit of the wavefront sensor, the SHWS measurement will break down. Fortunately, the GFP-tagged centrosome proteins are smaller than the diffraction limit of the wavefront sensor.

2.5 Wavefront measurement and PSF estimation

Before wavefront measurement, a reference image was captured using the wavefront sensor with a collimated laser beam added to the optical path after the DM. The positions of the spots in the image were detected using a cross-correlation centroiding algorithm [15]. During wavefront measurement, the wavefront slopes are determined from the measurement of the spot displacements in the image, which was implemented using Visual C++ 2010 (Microsoft Corporation). This information is required for online control of the deformable mirror. To obtain a whole wavefront, a fast Fourier transform reconstruction algorithm is implemented using MATLAB (MathWorks) [19]. The wavefront can be further decomposed into different Zernike polynomial terms by least square fitting [3]. Different polynomial terms correspond to different aberration modes. The first 15 terms are shown in Table 1. The program is interfaced with the main program through a MATLAB Engine. The intensity of the PSF is obtained by [20]

$$PSF = \left|h_{ill}\right|^2 \left|h_{col}\right|^2 \qquad (4)$$

#166370 - $15.00 USD Received 23 Apr 2012; revised 18 Jun 2012; accepted 19 Jun 2012; published 28 Jun 2012

where h_{ill} and h_{col} are the coherent illumination and detection PSFs. They can be calculated numerically by the non-paraxial amplitude PSF for high numerical aperture using MATLAB (MathWorks) [20]. Because of the time required, this estimation operates off-line. In this paper, the Strehl ratio is used to measure the optical quality of the system. It was calculated based on the estimated PSF by the ratio of peak intensities in the aberrated and ideal PSF [3]. The radius of the PSF with 80% encircled energy is used to measure the size of the PSF.

2.6 The measurement noise for the SHWS

The measurement noise of the wavefront sensor is related to the signal to noise ratio (SNR) of the camera, which can be estimated using [21]

$$\sigma_m = \sqrt{2}\frac{\pi^2 K_g}{4(SNR)}\left[\left(\frac{3}{2}\right)^2 + \left(\frac{\theta d}{\lambda}\right)^2\right] \tag{5}$$

where K_g is a constant to account for centroiding errors due to the fill factor on the CCD. θ is the angular radius of the spot size. λ is the wavelength of the excitation light. d is the sub-aperture diameter. The signal to noise ratio of a detector is given by

$$SNR = \frac{n_p}{\sqrt{n_p + N_D[n_B^2 + (e/G)^2]}} \tag{6}$$

where n_p is the number of detected photoelectrons per sub-aperture, N_D is the number of detector pixels per sub-aperture. n_B is the number of detected background electrons per pixel. e is the read noise. G is the intensifier gain. For the current system, the measurement noise in terms of root mean square (RMS) error calculated by Eq. (5) and (6) for different depths is shown in Fig. 3. The laser power was set to 150 μw at the back aperture of the objective lens during wavefront sensing. The exposure time changes from 10 ms to 50 ms. At a depth of 90 μm, the measurement noise is around 0.074 λ (λ = 509 nm) with an exposure time of 50 ms. The scattering effect becomes much stronger at around 90 μm depth, which induces a large drop in the absolute signal measured.

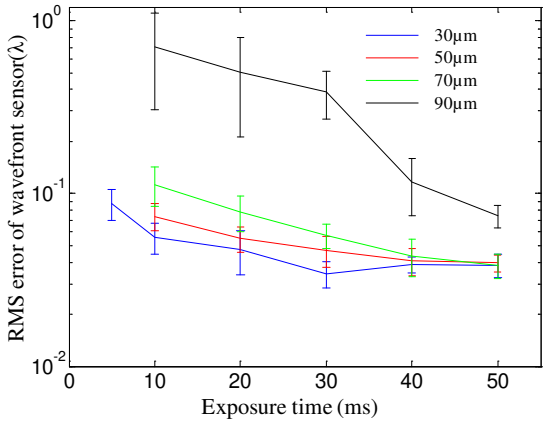

Fig. 3. Measurement noise change with the exposure time at different depths. The error bar is the standard deviation for 10 measurements.

2.7 Spatial filter setting to block the light from out of focus planes

The light from the out of focus planes adds noise to the wavefront measurement. A spatial filter (SF) can be placed at the focusing plane between the relay lenses in front of the wavefront sensor. However the SF also removes high-order wavefront from the sample. Fortunately, for most biological tissues, higher-order Zernike modes give only a small

#166370 - $15.00 USD Received 23 Apr 2012; revised 18 Jun 2012; accepted 19 Jun 2012; published 28 Jun 2012

contribution to the overall aberration [22]. For the *Drosophila* embryo, the first 14 Zernike modes (without piston, tip, and tilt) give the major contributions [23]. The size of the pinhole can be determined from the band-limit of the wavefront measurement, which depends on the number of the Zernike modes to be measured [3]. 14 lenslets are the minimum number for a reliable measurement of the aberrations up to the first 14 Zernike modes. The measured wavefront is bandwidth limited at $1/2d_{sub}$ because of aliasing [24], where d_{sub} is the width of the sub-aperture. A spatial filter with a width of λ/d_{sub} can attenuate the high-spatial frequency content above $1/2d_{sub}$. With an aperture of 4 mm, d_{sub} for 14 lenslets is 0.85 mm. The angular size of the spatial filter is 6×10^{-4} rad for $\lambda = 509$ nm, which corresponds to a pinhole size of 150 µm.

2.7 Sample preparation

UAS EGFP-Cnn; Nanos-Gal4 flies [25] and GFP-Polo flies, where GFP is cloned into the 5′ coding region of the Polo gene [26], were reared on standard cornmeal and molasses media. Embryos were collected for one hour on grape juice agar then aged at room temperature for 30-60 minutes. Dechorionation was done by hand using double-sided tape and embryos were adhered to coverslips. Embryos were covered in Halocarbon oil (Sigma) to allow oxygen permeation and inhibit desiccation [27].

3. Experiment

3.1 Wavefront measurement and correction

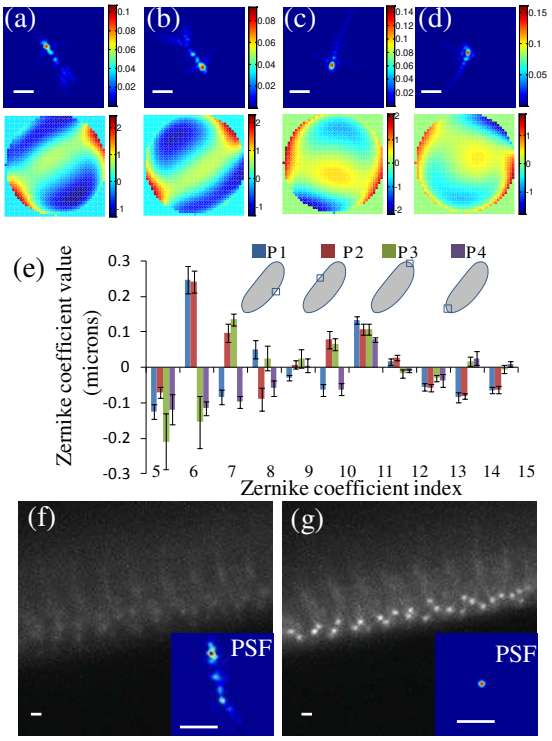

Fig. 4. Wavefront measurement and correction. (a-d) The averaged point spread function (PSF) and wavefront errors over 6 measurements using EGFP-Cnn labeled centrosomes of a cycle 14 Drosophila embryo at four different locations (P1, P2, P3 and P4) at a depth of 60 µm. (e) The averaged coefficient value of the first 15 Zernike polynomial modes at these four locations. The error bar is the standard deviation for 6 measurements. (f-g) The images and PSF without and with correction for a cycle 14 Drosophila embryo with GFP-polo at a depth of 83 µm. Scale bars, 2 µm.

#166370 - $15.00 USD Received 23 Apr 2012; revised 18 Jun 2012; accepted 19 Jun 2012; published 28 Jun 2012

The ability for making a wavefront measurement using FPCGS was tested for measurement of spatially dependent wavefront aberrations from the Drosophila embryo with EGFP-Cnn labeled centrosomes at four different positions as shown in Figs. 4(a-d). In the experiments in this paper, we are looking at the outer edge of an ovoid shaped embryo and therefore a small fraction of the distance is through cytoplasm and the other fraction is through the mounting medium. The illumination PSF and corresponding wavefront error show its high dependence on the sample orientation and imaging location. To analyze the specific aberrations, the wavefront measurements can be decomposed into different Zernike polynomials as shown in Fig. 4(e). In contrast to mouse brain tissue [11], where spherical aberrations are the dominant aberrations, the curved edge of the *Drosophila* embryo induces a large amount of astigmatism (modes 5 and 6) aberrations because of its cylindrical shape. The signs of these modes change according to the location. Those measurements also verified the necessity to correct these spatially dependent aberrations using adaptive optics. The results of these corrections are shown in confocal microscopy images without and with corrections that are captured at a depth of 83 μm below the coverslip, as shown in Figs. 4(f-g). The GFP-polo labeled centrosomes can be observed clearly after correction but cannot be observed before correction. The size of the PSF decreases from 1.7 μm to 0.21 μm. The Strehl ratio calculated based on the PSF shows an increase from 3.3×10^{-3} to 0.7.

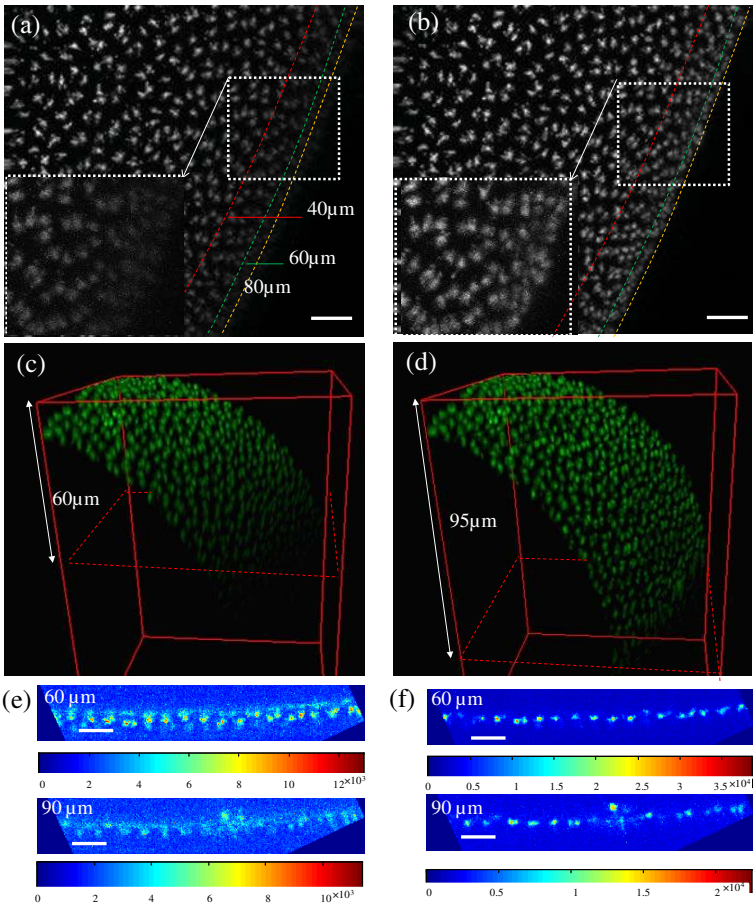

Fig. 5. Comparison of the three-dimensional imaging without and with correction for imaging of cycle 13 fly embryos with EGFP-Cnn label. (a-b) The maximum intensity projection of the scan series from the top surface to 100 μm without and with AO (Media 1). (c-d) The 3D reconstructions without and with AO. (e-f) The confocal images without and with AO at the depths of 60 μm and 90 μm. The color maps are scaled to show the image data over its full range. Scale bar, 10 μm.

#166370 - $15.00 USD Received 23 Apr 2012; revised 18 Jun 2012; accepted 19 Jun 2012; published 28 Jun 2012

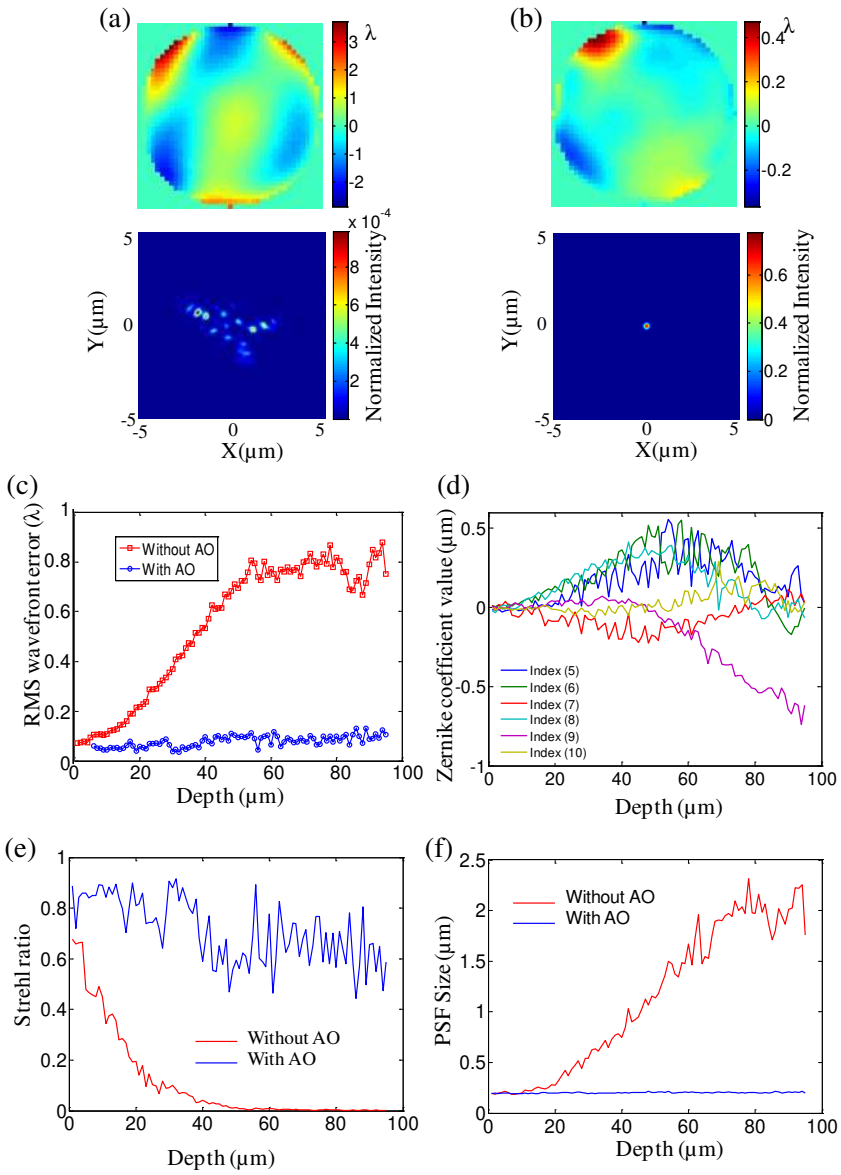

Fig. 6. Comparison of the wavefront measurements and the PSFs without and with AO for different depths. (a-b) The wavefront measurements and PSF without and with AO at the depth of 90 μm (Media 2). (c) The RMS wavefront errors change with the depth. The red and blue lines indicate the measurement without and with AO respectively. (d) The Zernike coefficient values without AO with the change of depth. (e-f) The Strehl ratio and PSF size change for different depths. The red and blue lines indicate without and with AO respectively. (λ = 509 nm)

3.2 Three-dimensional imaging with wavefront correction

The penetration depth of the AOM for live imaging of a *Drosophila* embryo is tested by performing AO correction during Z scanning from the top surface to a depth of 100 μm below the coverslip with a 1 μm z-step size . The correction is performed at each z-step. The purpose of the guide-star searching algorithm is to search and calculate the location of EGFP-Cnn at each depth, acting as a potential guide-star, in a cycle 13 embryo. Figures 5(a, b) show

#166370 - $15.00 USD Received 23 Apr 2012; revised 18 Jun 2012; accepted 19 Jun 2012; published 28 Jun 2012

the maximum intensity projection produced from a scan series (Media 1) without and with correction respectively. The GFP at the edge of embryo at different depths can be observed. Before correction, the EGFP-Cnn labeled centrosomes can only be observed down to 60 µm in depth. After correction, they can be observed below a depth of 80 µm. Using the 3D view function in ImageJ with a re-sampling factor of 2, the 3D images of the *Drosophila* embryo show the imaging depth increases from 60 µm to 95µm, with more than a 50% increase in imaging depth as shown in Figs. 5(c, d). Figures 5(e) and (f) show the enlarged images without and with correction at depths of 60 µm and 90 µm, respectively.

At each depth, the wavefront error is measured before correction. After correction, the wavefront is measured again directly from the sample with an updated correction by the DM. Then PSFs are calculated from the wavefront measurements (Media 2). Figures 6(a) and 6(b) show the wavefront measurement and estimated PSF at a depth of 90 µm below the coverslip without and with correction respectively. The RMS wavefront errors at different depths with and without correction are shown in Fig. 6(c). Without correction, the RMS wavefront error reaches approximately 0.8λ when the imaging depth goes to 90 µm. The Zernike coefficient values without AO with the change of depth are shown in Fig. 6(d). Below a depth of 50 µm, the astigmatism and coma aberrations (index 5,6,7 and 8) begin to decrease with the increase of trefoil x aberration (index 9). Those contribute a RMS wavefront error of around 0.8 λ from 50 µm to 90 µm. However the increases in the high order aberration (the third order) generates a larger PSF with an increase in depth. The decrease of the Strehl ratio in Fig. 6(e) shows the degradation of the optical performance with the imaging depth. After correction, even at a depth of 90 µm, the system can still achieve a Strehl ratio of 0.6 with an RMS wavefront error of 0.1λ. Aside from improving the penetration depth, AOM also improves the optical resolution. Although the EGFP-Cnn labeled centrosomes can be observed at a depth of 60 µm without AO, the resolution is still poor because of the aberrations as shown in Figs. 5(e) and 5(f). Before correction, the size of the PSF is 1.67 µm at a depth of 60 µm. After correction, it decreases to 0.22 µm as shown in Fig. 6(f). At a depth of 90 µm, it shows a significant improvement of the PSF by a factor of nine.

3.3 Time lapse four dimensional (4D) imaging

Enabled by the fast wavefront measurement and correction ability, the AOM using FPCGS can be used for time lapse 4D imaging. Here we recorded the EGFP-Cnn labeled centrosomes of an early *Drosophila* embryo for 4D imaging at a depth of 80 µm with an image size of 512x512 pixels and a time resolution of 30 s for five consecutive focal planes (1 plane/µm) over 20 minutes. At the beginning of each time period, the wavefront error is corrected at the third focal plane. In every time interval, images with and without correction are collected sequentially for comparing the results. The wavefront errors are measured directly from the sample before and after correction respectively. The image sequence with a frame rate of 30 s was achieved by the maximum intensity projection in each time period. A single frame without and with correction of the video movie (Media 3) is shown in Fig. 7(a). It shows a significant improvement in contrast and resolution. Without correction, the measured wavefront shows a dynamic change during the imaging time (Media 4). The variation of the wavefront can also be seen from the coefficient value change of different Zernike modes as shown in Fig. 7(b). The short term data with 20 minutes imaging time is dominated by noise, which comes from the measurement noise of the wavefront sensor because of low-level photon emission. The enlarged PSF with a size around 1.8 µm makes it impossible to obtain high resolution images. After correction, the coefficient value for Zernike modes are all below 0.05 µm. The Strehl ratio increases to around 0.6 as shown in Fig. 7(c). The AO compensates those dynamic aberrations and produces a near perfect PSF with a spot size of 0.22 µm as shown in Fig. 7(d) (Media 4).

#166370 - $15.00 USD Received 23 Apr 2012; revised 18 Jun 2012; accepted 19 Jun 2012; published 28 Jun 2012

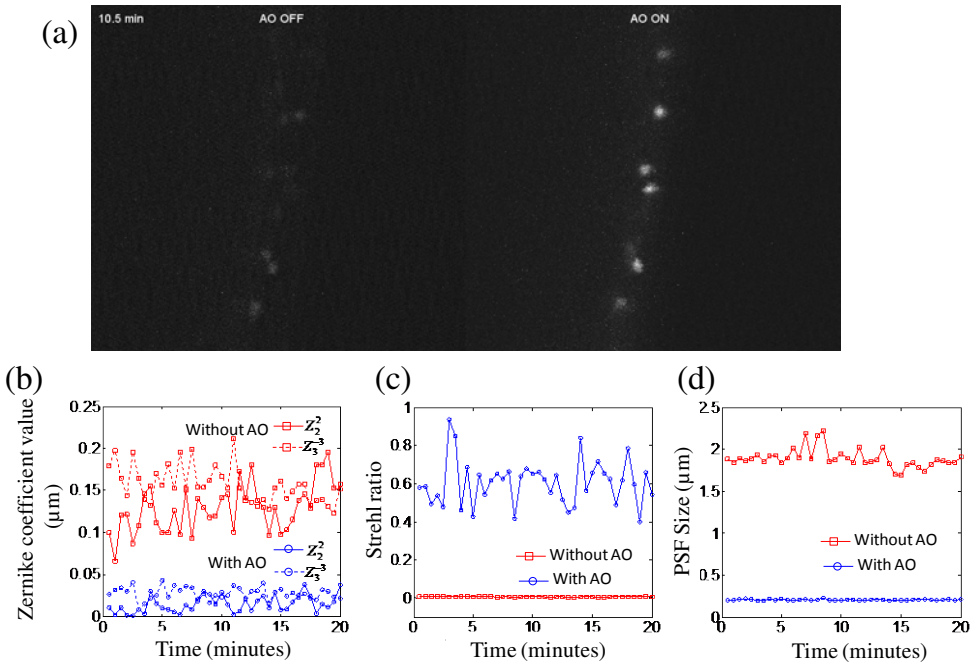

Fig. 7. 4D imaging of cycle 13 fly embryos with EGFP-Cnn label at depth of 80 μm. (a) A single frame without and with correction of a video movie (Media 3). (b) The coefficient value changes for Zernike modes Z_2^2 (Astigmatism x, dashed line) and Z_3^{-3} (Trefoil y, solid line) with and without AO during 20 minutes. (c) The Strehl ratio change with (blue) and without (red) AO during 20 minutes. (d) PSF size change with (blue) and without (red) AO during 20 minutes (Media 4).

4. Conclusion

In summary, AO microscopy with a direct wavefront sensing method using FPCGS can correct for the aberrations induced by the ovoid shape of the Drosophila embryo at high resolution for live imaging. Compared to the use of a fluorescent microsphere as a reference guide-star [10, 21], using FP labeled in sub-cellular structures as a noninvasive method simplifies the tissue preparation process and avoids the potential side effects in live imaging. The guide-star could be the same FP for imaging or specially designed proteins for use only as a guide-star. A FP such as td-Tomato with high quantum yield, less photobleaching and more stability will further extend the correction depth and provide a more robust wavefront correction for live imaging. Using FPs with an excitation wavelength different from the imaging FPs can avoid the need to switch the light path between the wavefront sensing and imaging paths. Of particular interest is the use of a centrosome as a guide-star. We can always find one or two centrosomes per cell in all animal cells depending on their position within the cell cycle. It broadens the applications of the direct wavefront sensing method for different kinds of cells and sample types. Moreover, the size of the centrosome is around 1 μm, which is particularly suitable as a guide-star for the SHWS. The centrosomes are usually located close to the nucleus. The separation of centrosomes in two cells is often large enough in three-dimensional space for wavefront measurement with less back ground noise and less influence from the neighboring guide-stars.

In comparison with the image-based AO method, the direct wavefront sensing method used here requires less time for wavefront measurement, which is particularly suitable to correct the dynamic aberration induced in live specimens. The total wavefront correction time is 600 ms which includes a 50 ms exposure time for wavefront measurement, a 50 ms DM control time and a 500 ms flipper mirror switching time. The last one can be minimized to

#166370 - $15.00 USD Received 23 Apr 2012; revised 18 Jun 2012; accepted 19 Jun 2012; published 28 Jun 2012

less than 1ms by using a fast steering mirror. To further minimize the DM control time, open loop control to update the DM using the wavefront measurement and an accurate DM model could be applied after the calibration of the DM. In this case, the correction speeds would be only limited by the wavefront measurement. Applying Field Programmable Gate Arrays (FPGA) in wavefront measurement will be beneficial for time-critical applications. For tissues with small isoplanatic patches [23], the guide-star searching algorithm could find the optimal local guide-star in each patch. The large field of view with correction can be provided by stitching those patches together. Finally, the application of FPCGS also simplifies the design of the hardware and software. Due to sharing a similar concept of wavefront sensing based on a laser guide-star in astronomy and vision science, the knowledge of AO application in those fields will facilitate its application in microscopy. The method we present here can be also applied to other fluorescence microscopes, such as wide-field microscopy, multi-photon microscopy or super-resolution microscopy.

Table 1. Zernike Polynomials used in this paper

Index (j)	$Z_n^m(\rho,\theta)$	Aberration mode
1	1	Bias
2	$2r\cos(\theta)$	Tilt x
3	$2r\sin(\theta)$	Tilt y
4	$\sqrt{3}(2r^2-1)$	Defocus
5	$\sqrt{6}r^2\cos(2\theta)$	Astigmatism x
6	$\sqrt{6}r^2\sin(2\theta)$	Astigmatism y
7	$2\sqrt{2}(3r^3-2r)\cos(\theta)$	Coma x
8	$2\sqrt{2}(3r^3-2r)\sin(\theta)$	Coma y
9	$2\sqrt{2}r^3\cos(3\theta)$	Trefoil x
10	$2\sqrt{2}r^3\sin(3\theta)$	Trefoil y
11	$\sqrt{5}(6r^4-6r^2+1)$	Primary Spherical
12	$\sqrt{10}(4r^4-3r^2)\cos(2\theta)$	Secondary Astigmatism x
13	$\sqrt{10}(4r^4-3r^2)\sin(2\theta)$	Secondary Astigmatism y
14	$\sqrt{10}r^4\cos(3\theta)$	Tetrafoil x
15	$\sqrt{10}r^4\sin(3\theta)$	Tetrafoil y

Acknowledgments

We acknowledge technical support from Ben Abrams in the UCSC Life Sciences Microscopy Center. We would also like to thank T. Megraw for the EGFP-Cnn flies and C. Sunkel for the GFP-Polo flies. This material is based upon work supported by the National Science Foundation (NSF) under Award No. 0852742, the W.M. Keck Center for Adaptive Optical Microscopy at UC Santa Cruz and the California Institute for Regenerative Medicine (CIRM), Grant #RT1-1095-1. The contents of this publication are solely the responsibility of the authors and do not necessarily represent the official views of CIRM or any other agency of the State of California. This work was also supported by a grant to W. S. from the National Institutes of Health (GM44757).